Mode-based Sensing and Actuation Techniques for Multi-objective Flexible Aircraft Control

Kelley E. Hashemi*
NASA Ames Research Center, Moffett Field, CA, 94035

Andrew Alder†
University of Colorado Boulder, Boulder, CO 80309

Nick Cramer‡ and Nhan T. Nguyen§
NASA Ames Research Center, Moffett Field, CA, 94035

Intelligent sensing and actuation designs are explored as a means to improve performance of a gust load alleviation control design for a flexible wing aircraft equipped with wing-shaping control surfaces. The proposed techniques rely on identification of the dominant structural modes during specified flight conditions and uses them as a basis for sensor placement and actuator utilization. Specifically, a strategy for sensor placement is discussed that uses target mode shape capture as a mean to improve state estimation quality. A second strategy that reduces the number of wing-shaping control inputs using mode and objective-based shape functions as virtual input channels is also presented. Both techniques are demonstrated in simulation of a flexible wing transport aircraft utilizing a multi-objective control system designed to suppress flexible motion, minimize gust and maneuver load, and reduce drag.

I. Introduction

TRANSPORT aircraft designs are moving towards the use of lightweight materials and less rigid geometries in pursuit of ever increasing fuel efficiency. New aircraft designs are more structurally flexible than their predecessors and are correspondingly more susceptible to disturbances such as gust. Active control techniques are being widely investigated as a means to both counteract the negative behaviors of flexible aircraft and to exploit the flexibility for performance gain. In this study we examine the multi-objective optimal controller previously developed by the authors [1], [2] as a technique to provide gust load alleviation (GLA) along with enabling potentially competing objectives of mode suppression, maneuver load alleviation, and drag minimization. Further, we seek to improve upon the performance of the control system by making intelligent sensing and actuation system design choices based on our knowledge of the structural modes.

The mode-based control system design choices are explored in simulation of a flexible aircraft wing based on the NASA Common Research Model (CRM) geometry and equipped the many degree-of-freedom trailing edge actuation system known as the Variable Camber Continuous Trailing Edge Flap (VCCTEF) [3], [4], [5]. On the actuation side, we present a method of reducing the number of control inputs using shape functions corresponding to mode shapes and objective achievement. On the sensing side, we explore a sensor placement technique that seeks to improve estimation of the modal states by selecting locations that respect flexible motion. Both approaches rely on identification and use of the mode shapes with highest participation which may vary based on the source of excitation.

The paper is organized as follows: Section II describes the wing, simulation model, and dominant mode shapes used for the present study. The multi-objective optimal controller used for demonstration of the sensing and actuation choices is reviewed in Section III. Section IV describes the mode and objective-based shape function actuation technique, while Section V contains the mode-cognizant sensor placement algorithm. Some concluding remarks are provided in Section VI.

*Research Scientist, Intelligent Systems Division, AIAA Member, kelley.e.hashemi@nasa.gov
†Graduate Student, Dept. of Aerospace Engineering Sciences
‡Research Scientist, Intelligent Systems Division, AIAA Member
§Technical Group Lead and Research Scientist, Intelligent Systems Division, AIAA Associate Fellow

Fig. 1 Wing under construction

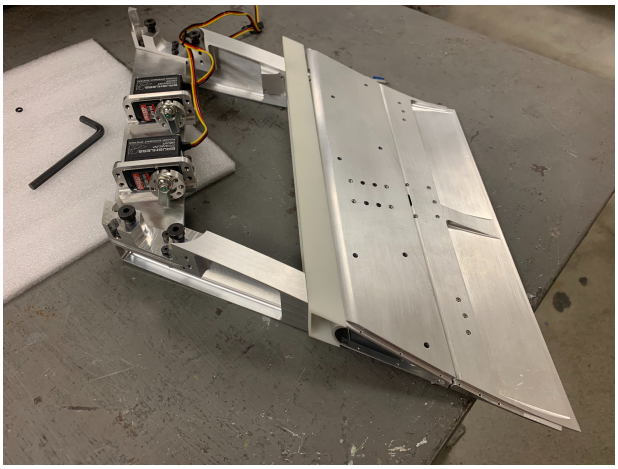

Fig. 2 VCCTEF flap under construction

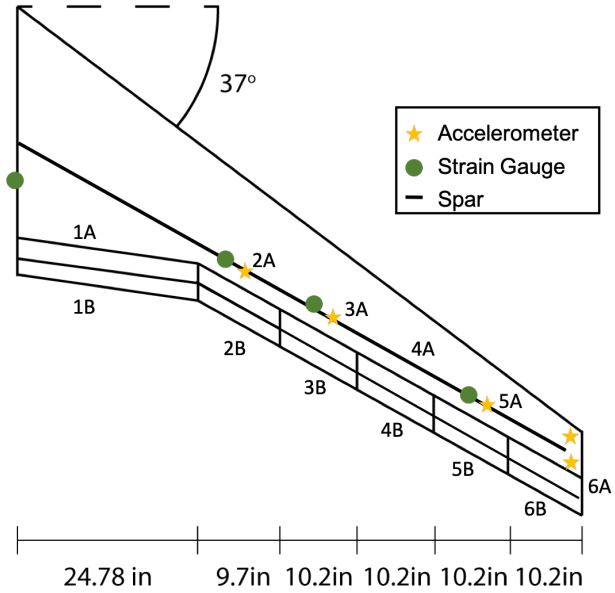

Fig. 3 Wing schematic indicating commandable flaps and sensor locations

II. Wing Description

A flexible wing adhering to the CRM geometry [6] is being constructed as part of NASA's Performance Adaptive Aeroelastic Wing project to demonstrate active multi-objective GLA techniques. The 7 ft half span wing includes VCCTEF actuation consisting of six individually actuated flaps and flexible inserts between flaps to provide a smooth trailing edge surface. Pictures of the wing and a flap during the construction process are provided in Fig. 1 and Fig. 2, respectively. Camber variation is available through the use of a secondary hinge. However, in this study only the secondary hinge is used (i.e. the **B** segments) as it is intended for faster response than the inner hinge. Sensors used by the control designs include multiple accelerometers and strain gauges. A schematic of the sensing and actuation mechanisms is depicted in Fig. 3. Upon completion the wing will be used to evaluate various GLA designs in a series of wind tunnel tests in the Kirsten Wind Tunnel (KWT) at the University of Washington Aeronautical Lab (UWAL). A gust generation system was recently installed at the KWT and is depicted in Fig. 4. It consists of four vanes that can be commanded to produce sinusoidal and discrete $(1 - \cos)$ gust profiles. Accordingly, the study at hand is restricted to analysis of sinusoidal gust disturbance response.

Fig. 4 UWAL gust generator installation

An aeroservoelastic (ASE) state space model of the wing was developed for the purpose of control design and simulation. The model includes both modal dynamics and unsteady aerodynamics. It also couples VCCTEF control action as well as gust dynamics to their behavior. Complete details of the modeling work can be found in [7]. This ASE model serves as the basis for the present investigation.

For the purposes of this study the wing should be excited by a low frequency, sinusoidal gust disturbance similar to that which UWAL gust generation system is expected to provide. The driving frequency is therefore restricted to a frequency at or near that of the first mode to ensure relevance to what can be feasibly executed in the tunnel while also ensuring clear mode excitation. The first few modes are expected to form the bulk of the response in this scenario and will be used as the target modes in the sensing and actuation schemes to be discussed. Their mode shapes are shown in Figs. 5 to 7.

III. Multi-objective Control Design

The dynamics of the gust-disturbed wing at specified flight conditions are given by

$$\dot{x} = Ax + B_m u_m + Ew \tag{1}$$

$$y = Cx + D_m u_m + Fw. \tag{2}$$

Here the state x includes modal displacements and velocities, aerodynamic lags and control surface lags. Note that rigid body dynamics are not included due to the experimental set up. The gust is indicated by the vector w which contains the vertical velocity and vertical acceleration of the disturbance impacting the wing. A multi-objective control term u_m is considered in this paper which can utilize any portion of the VCCTEF control surfaces. Outputs of the system include the previously indicated strain gauges and accelerometers.

Relevant performance metrics can be expressed as follows: Wing root bending moment is given by

$$M_y = M_x x + M_{u_m} u_m + M_w w. \tag{3}$$

The change in drag from an optimized baseline configuration is

$$\Delta C_D = C_{D_x} x + C_{D_{u_m}} u_m + x^T C_{D_{x^2}} x + x^T C_{D_{xm}} u_m + {u_m}^T C_{D_{u^2 mm}} u_m. \tag{4}$$

Note that ΔC_D will always be positive due to a drag-optimized choice of baseline.

Each mode-based improvement begins from same multi-objective optimal control design that addresses flexible motion stabilization, gust and maneuver load alleviation, and drag minimization. This optimal controller is given by the input u_m that minimizes the cost function

$$J = \lim_{t_f \to \infty} \frac{1}{2} \int_0^{tf} \left(x^T Q x + u_m^T R_m u_m + q_M M_y^2 + q_D \Delta C_D \right) dt \tag{5}$$

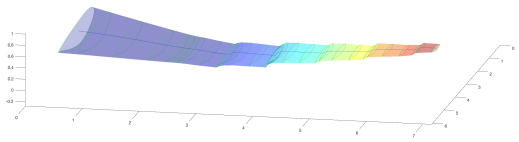

Fig. 5 Mode 1 (2.8 Hz)

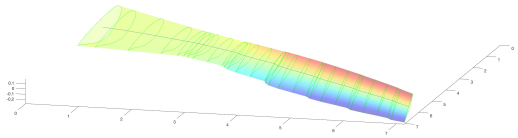

Fig. 6 Model 2 (13.78 Hz)

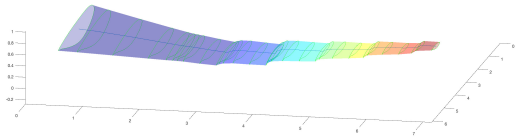

Fig. 7 Mode 3 (15.0 Hz)

subject to the dynamic constraint of the state in Eq. (1) and the performance terms in Eq. (3) and Eq. (4). Q, R_m, q_M, are q_D are appropriately-sized user-selected weights. The resulting controller has the form

$$u_m = K_x \hat{x} + K_w \hat{w} + \Lambda. \tag{6}$$

The derivation of this control law is discussed in greater detail in [2] and gain definitions can be found in the Appendix. Note that an observer must be used to obtain an estimate of the state $\hat{x}$ for implementation of u_m. More importantly, an estimate of the gust $\hat{w}$ must also be obtained. A study discussing gust estimation techniques for this wing is included in [8] and further details are omitted here.

IV. Actuation: Mode and Objective-based Shape Functions

Although use of the VCCTEF for actuation provides a large number of degrees of freedom, the high number of control channels can be a computational burden for MIMO control techniques. Further, individually commanding each segment of the VCCTEF could lead to non-smooth shapes for the trailing edge that might increase drag or damage the flexible inserts between segments. One potential remedy is to reduce the number of control input channels through the use of a shape function. A shape function utilizes a small number of commandable degrees of freedom, known as virtual inputs. The virtual inputs replace the original inputs as the command channels of the plant. Specified values of the virtual inputs define a profile, or shape, that spans the length of the wing. The shape is then used to recover the actual control inputs. Use of a shape function therefore aids in ensuring a smooth a smooth VCCTEF surface as well as reducing the number of input channels.

A. Shape function options

Previous VCCTEF investigations have examined the use of shape functions defined by characteristic polynomials [2]. Specifically, smooth results have been reliably obtained using Chebyshev polynomials. This paper also investigates the novel use of shape functions based on mode shapes as well as shape functions based on profiles known to facilitate certain objectives. Each of the shape function options is discuss in more detail subsequently.

1. Chebyshev polynomials

Previous VCCTEF work utilized a 4th-order Chebyshev polynomial to reduce the number of control channels and pursue smooth trailing edge profiles

$$\delta_i = c_0 + c_1 k + c_2(2k^2 - 1) + c_3(4k^3 - 3k). \tag{7}$$

For n_u original inputs and 4 virtual inputs, $k = \frac{i-1}{n-1}$ for $i = 1...n_u$. The deflection of the i^{th} VCCTEF segment is δ_i, and c_j for $j = 0...3$ are the virtual control variables. In other words, at each instant the VCCTEF deflection profile is a linear combination of the four polynomials illustrated in Fig. 8.

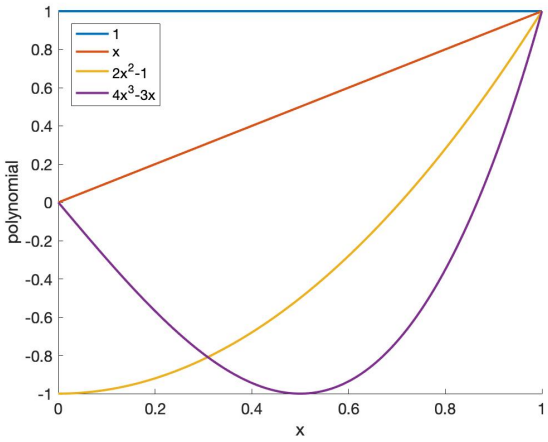

Fig. 8 First four Chebyshev polynomials

2. Modes

Next, consider using dominant mode shapes as the polynomials that constitute the basis of the shape function. Given the orientation of the gust generation system and the low frequency disturbance expectations, we elect to use only the first two bending modes–modes 1 and 3, shown in Fig. 9–for this construction. VCCTEF deflections are given by

$$\delta_i = c_0\,(\text{Mode}_{1i}) + c_1\,(\text{Mode}_{3i}) \tag{8}$$

where Mode_{1i} indicates the normalized displacement of the first mode at the location of the i^{th} VCCTEF segment. Similar to the Chebyshev case, c_0 and c_1 are the two virtual control variables.

3. Objectives

The last option considered replaces the polynomials used in shape function construction with profiles that are generally considered effective for achieving specified objectives. Here the multi-objective controller is already attempting to suppress flexible motion and minimize drag, among other concerns, and profiles facilitating these two particular objectives have been selected in an attempt to amplify the effect. VCCTEF deflections are given by

$$\delta_i = c_0\,(\text{Obj}_{1i}) + c_1\,(\text{Obj}_{2i}) \tag{9}$$

where Obj_{1i} indicates the normalized displacement of the first objective's profile at the location of the i^{th} VCCTEF segment, and c_0 and c_1 are two virtual control variables. Taking the first objective to be flexible motion suppression, we choose the profile

$$\text{Obj}_1 = 2x \tag{10}$$

as it emphasizes deflection of the outboard control surfaces. These surfaces are often considered to be most effective for flutter suppression and related tasks. Making drag minimization the second objective, a profile that emphasizes use of the inboard control surfaces and mimics the drag-optimal elliptical lift distribution is selected

$$\text{Obj}_2 = \sqrt{1 - \left(\frac{2x}{b}\right)^2}. \tag{11}$$

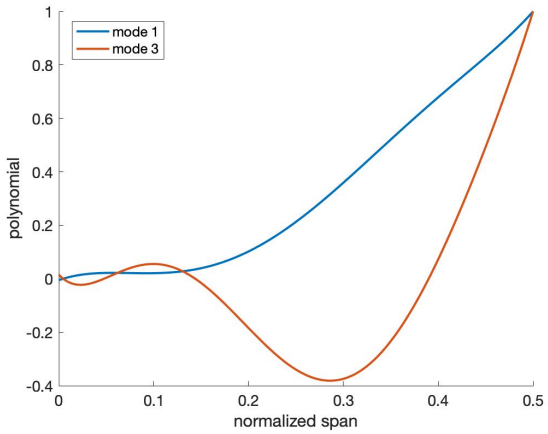

Fig. 9 Mode-based shape function components

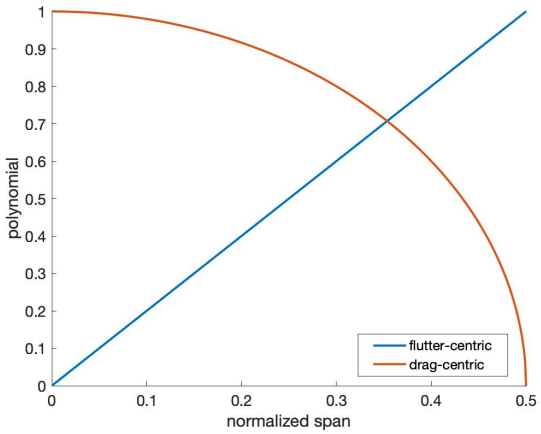

Fig. 10 Objective-based shape function components

Both profiles are shown in Fig. 10.

B. Performance comparison

Efficacy of the shape functions is evaluated using a gust-disturbed simulation of the wing. The disturbance is specified by a 2.7 Hz sinusoidal gust profile with vertical 2 [m/s] amplitude. The multi-objective controller is implemented to pursue modal suppression, load alleviation, and drag minimization. It utilizes the six **B** flaps through the relevant mapping from virtual control variables for the active shape function. Multi-objective cost function weights are selected and held constant throughout all cases. Actuator dynamics are enforced on the control surface commands, though other realistic considerations such a modeling error and noise are not included.

The shape functions are implemented in an effort to ensure a smooth trailing edge profile for the wing, here taken to be <2° difference between adjacent VCCTEF segments. The shape functions should also either help the multi-objective controller improve upon its modal suppression/load alleviation/drag minimization performance with similar control surface motion, or achieve similar goal performance with smaller control surface motion. The smoothness and performance factors must be jointly considered to evaluate the usefulness of a particular shape function.

Results of a simulation comparing performance of the Chebyshev, mode, objective, and no shape function are presented in Figs. 11 to 14. Smoothness of the trailing edge is captured by Fig. 11 which shows the deflection difference between adjacent flaps. Note that only the objective shape function is consistently better than the use of no shape function. However, both the Chebyshev and objective shape functions keep relative deflections less that 2°, and the mode shape function very nearly meets this requirement. As for the performance goals, suppression of the first mode is most critical for the selected gust profile, and Fig. 13 indicates the most success when using the Chebyshev and objective shape functions. Load alleviation is captured by reduction in the wing root bending moment, shown in Fig. 14, and is facilitated best by the mode shape function. Drag minimization is evaluated based on minimizing the ΔC_D induced by multi-objective controller actuation since the baseline wing configuration is already optimized for drag. Thus, Fig. 14 indicates that only the mode shape function is preferable to no shape function.

The smoothness and performance factors suggest no clear choice of shape function, though the objective and mode options are both frequent standouts. However, Fig. 12 indicates that the absolute control surface deflections are generally smaller with the mode shape function than with the objective shape function, making the mode option preferable.

C. Alternate objective-based shape function

Given the lesser performance of the objective shape function, the choice of basis profiles was revisited and more tailored profiles were selected from related literature. Ref. 9 details an optimization study on a similar, though not identical, CRM wing geometry with control surfaces along the length of the trailing edge. It details the numerically optimized deflection profiles of the many trailing edge control surfaces for various objectives such as load alleviation and active flutter suppression. We generalized and smoothed the deflection profiles for these two objectives, shown in Fig. 15, and used them instead of the originally selected profiles to populate Eq. (9). Note that the original drag minimization

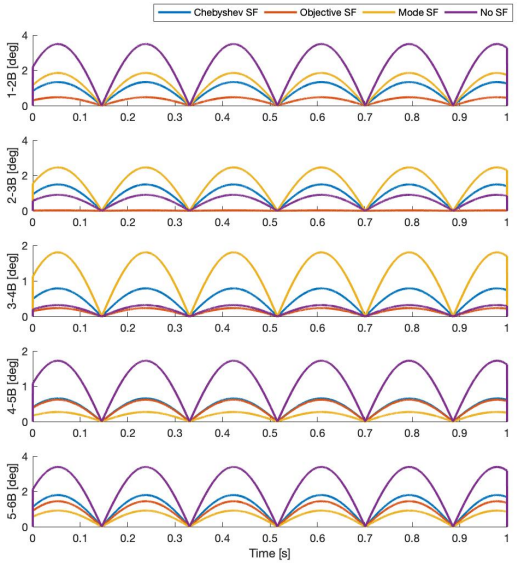

Fig. 11 Relative flap deflections for each shape function

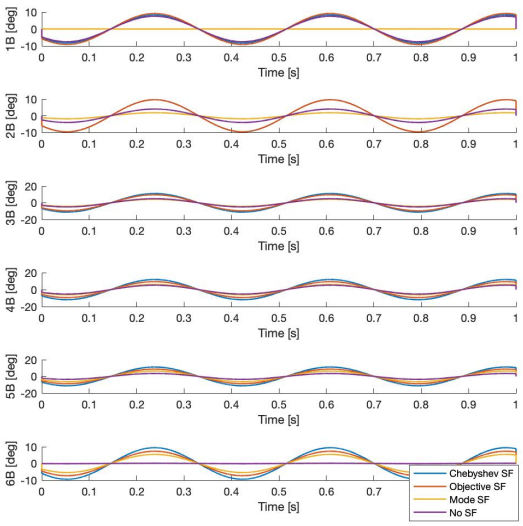

Fig. 12 Actual flap deflections for each shape function

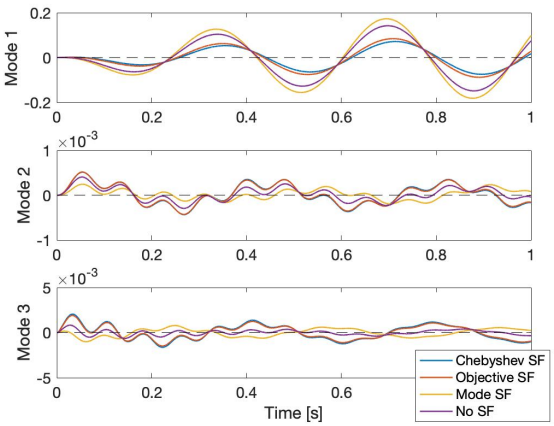

Fig. 13 Mode displacements for each shape function

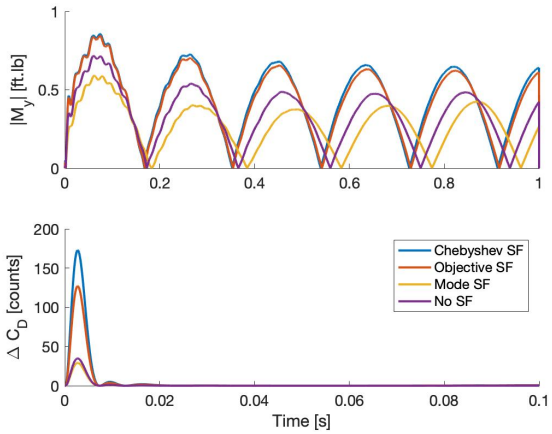

Fig. 14 Performance metrics for each shape function

focus was dropped in favor of load alleviation focus to make use the results readily available in the reference paper.

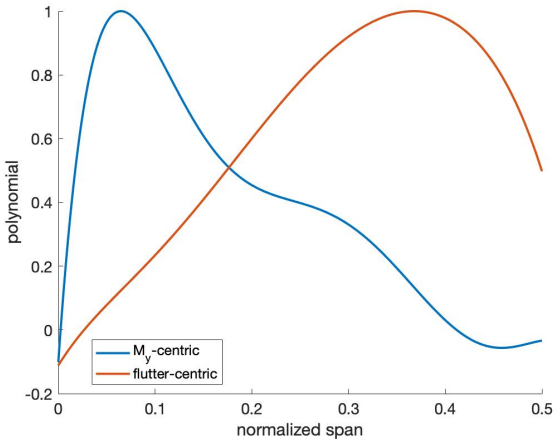

Fig. 15 Alternate objective-based shape function components

Results of the same suite of simulations, now with the alternate objective shape function, are presented in Figs. 16 to 19. The objective shape function has larger deflections between segments, shown in Fig. 16, and does not always meet the 2° requirement. Figure 18 indicates that the objective shape function's suppression of mode 1 is incrementally worse. However, load alleviation and drag minimization are improved as shown in Fig. 19. Figure 17 also shows that absolute flap deflections are favorably decreased. Though some factors are improved by use of the alternate objective shape function, the change is unlikely to be motivational given the initial effort required to determine the profiles used to construct the shape function.

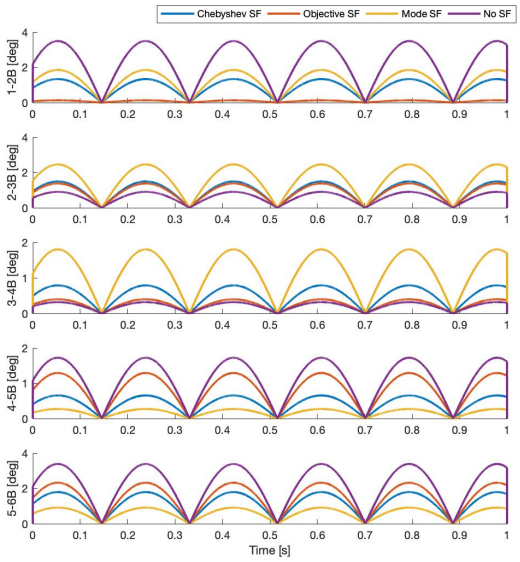

Fig. 16 Relative flap deflections, alternate objective shape function

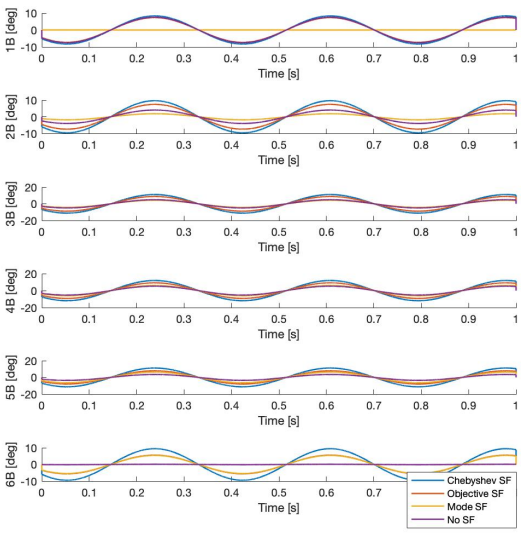

Fig. 17 Actual flap deflections, alternate objective shape function

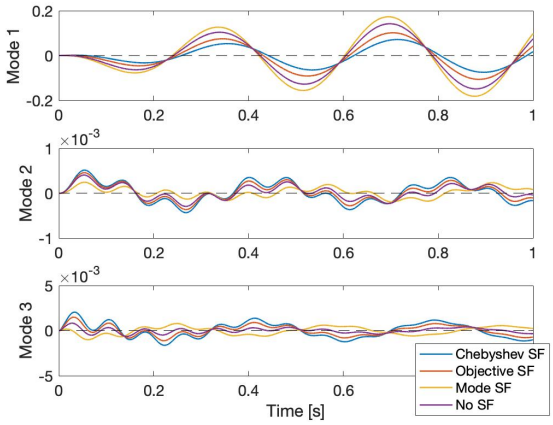

Fig. 18 Mode displacements, alternate objective shape function

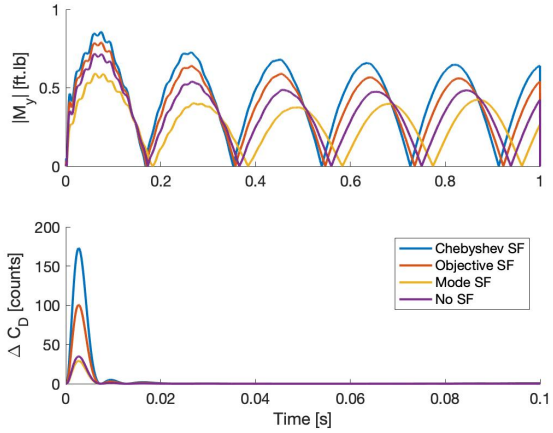

Fig. 19 Performance metrics, alternate objective shape function

V. Sensing: Mode-based Sensor Placement

It is also possible to involve mode shapes in the placement of sensors on the wing. Ideally, well-placed sensors can facilitate accurate estimation of the modal states. Several mode-based sensor placement techniques have been developed, and some have been effectively used on flexible space structures. Here we seek to adapt one such implementation, described in [10], for use with flexible aircraft.

A. Location selection algorithm

The reference describes the following iterative procedure:

1) Target modes (i.e. modes expected to strongly participate) and the set of all possible sensor locations are identified.
2) Sensor locations are ranked according to how much they contribute to the linear independence of target modes.
3) Location(s) that fall below a threshold of independence contribution are discarded.
4) The procedure is iterated until the desired number of sensors or other stopping criteria is met.

To accomplish the necessary ranking the algorithm depends on the matrix of FEM target modes partitioned to each of the sensor locations, denoted as Φ_s. Sensor output is expressed as

$$y = \Phi_s q \tag{12}$$

and the corresponding estimate of modal coordinates as

$$\hat{q} = \left(\Phi_s^T \Phi_s\right)^{-1} \Phi_s y. \tag{13}$$

The covariance matrix of the estimate error can be written as

$$P = \left(\Phi_s^T \Psi_0^{-2} \Phi_s\right)^{-1} \tag{14}$$

and is used to define the Fisher information matrix

$$Q = P^{-1} = \frac{1}{\Psi_0^2} \Phi_s^T \Phi_s = \frac{1}{\Psi_0^2} \sum_{i=1}^{m} \Phi_s^{iT} \Phi_s^i \tag{15}$$

where m is the number of sensors in the candidate set. Minimizing the covariance, which gives the best estimate, is equivalent to maximizing Q. The summation highlights that each of the m sensors has the ability to add value to Q. The number of sensors can be reduced while still keeping Q sufficiently "large" by removing sensor locations that do not contribute significantly. Further, the effective independence matrix can be constructed according to

$$E = \Phi_s \left(\Phi_s^T \Phi_s\right)^{-1} \Phi_s^T. \tag{16}$$

Here the i^{th} diagonal entry conveys the contribution of the i^{th} sensor to the rank of Φ_s, or equivalently the linear independence of the target modes.

B. Implementation results

A set of 30 equally spaced locations along the wing's spar have been identified as the candidate sensor placement locations. Each location has six degrees of freedom (DoFs), measurement of which can be mostly accomplished by a 3-axis accelerometers and gyroscopes, making a total of 180 DoFs. The first three modes were specified as the target modes due to the expected low frequency gust disturbance. The described algorithm was used to determine how few DoFs, and therefore sensors, could be retained and still achieve high target mode estimation accuracy.

Performance of the algorithm was tracked by removing the lowest contributing DoF in the current iteration and designing an estimator based on the sensors associated with the remaining DoFs. An open loop simulation with the wing disturbed 2.8 Hz, 2 [m/s] amplitude sinusoidal gust was then performed to capture the RMS error associated with each target mode's displacement estimate. As illustrated in Fig. 20 the estimation error stays consistent until 40 DoFs remain–equivalent to 21 sensor locations–at which point the estimate's RMS error begins to increase.

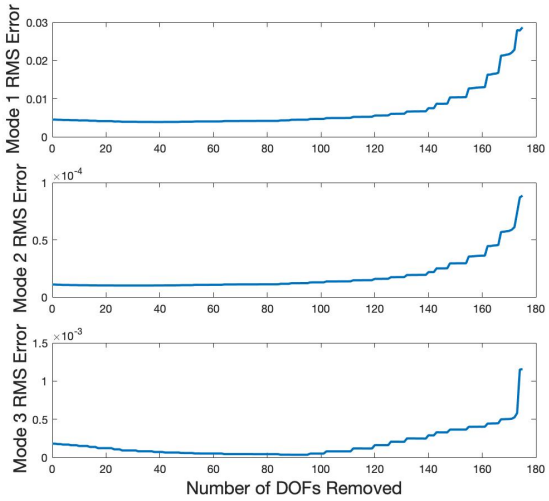

Fig. 20 Modal estimation error as a function of the number of DoFs removed

The target mode estimation accuracy from an open loop simulation utilizing the 21 optimized sensor locations is presented in Fig. 21. Estimation accuracy from a similar simulation utilizing the original accelerometers and strain gauges depicted in Fig. 3 is shown in Fig. 22. In both cases the simulation propagates a 20-mode version of the wing as the true dynamics while the observer is uses a reduced 5-mode version of the wing. Actuator dynamics and sensor noise are also included. The optimized sensor location version clearly provides more accurate estimation results, especially for modes 1 and 2. However, performance with the original sensor locations is not that much worse. The effort to install the additional sensors might not be worthwhile for this purpose.

VI. Conclusion

The present study described an aeroelastic wing model–equipped with a wing-spanning, many-segmented flap actuation mechanism and subject to a multi-objective control scheme–being developed for wind tunnel testing. The corresponding simulation model was used to establish the usefulness of a shape function actuation strategy that reduces the number of control inputs while encouraging a smooth profile of flap segments. Simulation results indicated that a mode-based version of the shape function strategy is preferable to the other options considered. Mode shapes were also used to implement an iterative sensor placement algorithm that uses target mode identification to guide down-selection of sensor locations. The sensor arrangement indicated by the algorithm resulted in highly accurate modal displacement estimates. Future efforts are aimed at incorporation of mode-based actuation strategy and sensor placement recommendations into the planned wind tunnel demonstrations. Extension of the mode-based sensing and

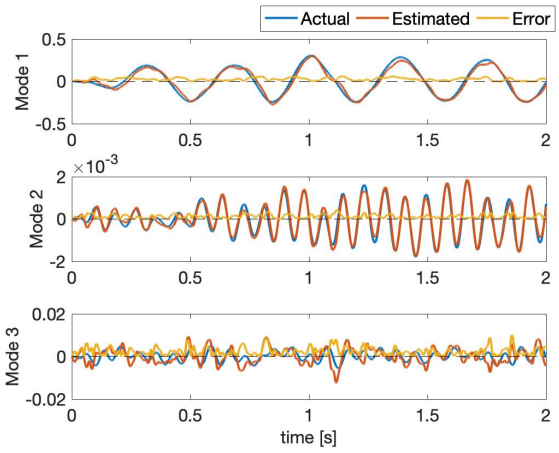

Fig. 21 Modal displacement estimation performance, optimized sensor locations

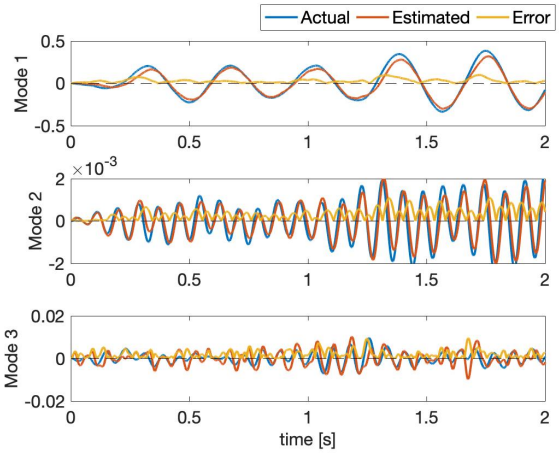

Fig. 22 Modal displacement estimation performance, original sensor locations

actuation strategies to additional wing geometries is also necessary to assess if the performance trends observed are generalizable.

Acknowledgments

This work was supported by the Advanced Air Transport Technology Project of the NASA Aeronautics Research Mission Directorate and a Phase III SBIR award to Scientific Systems Company, Inc. and the University of Washington Aeronautical Laboratory. Andrew Alder's participation was facilitated by the NASA International Internship Program and funded by a scholarship from the New Zealand Space Agency.

Appendix: Gain Definitions

The u_m gains in Eq. (6) require several nested definitions. They are summarized in reverse implementation order here, where W is the solution of the Riccati equation in Eq. (20).

$$K_x = -\bar{R}^{-1}\left(\frac{1}{2}q_D C_{D_{xu_m}}^T + q_M M_{u_m}^T M_x + B_m^T W\right) \tag{17}$$

$$K_w = -\bar{R}^{-1}\left(q_M M_{u_m}^T M_w + B_m^T V_w\right) \tag{18}$$

$$\Lambda = -\bar{R}^{-1}\left(\frac{1}{2}q_D C_{D_{u_m}}^T + B_m^T V_0\right) \tag{19}$$

$$W\bar{\bar{A}} + \bar{\bar{A}}^T W - W B_m \bar{R}^{-1} B_m W + \bar{\bar{Q}} = 0 \tag{20}$$

$$V_w = -\bar{\bar{V}}^{-1}\left[WE + q_M \bar{M}_x^T M_w - W B_m \bar{R}^{-1}\left(q_M M_{u_m}^T M_w\right) - \left(\frac{1}{2}q_D C_{D_{xu_m}} + q_M M_x^T M_{u_m}\right)\bar{R}^{-1}\left(q_M M_{u_m}^T M_w\right)\right] \tag{21}$$

$$V_0 = -\bar{\bar{V}}^{-1}\left[\frac{1}{2}q_D C_{D_x}^T - W B_m \bar{R}^{-1}\left(\frac{1}{2}q_D C_{D_{u_m}}^T\right) - \left(\frac{1}{2}q_D C_{D_{xu_m}} + q_M M_x^T M_{u_m}\right)\bar{R}^{-1}\left(\frac{1}{2}q_D C_{D_{u_m}}^T\right)\right] \tag{22}$$

$$\bar{\bar{V}} = \bar{\bar{A}}^T - W B_m \bar{R}^{-1} B_m \tag{23}$$

$$\bar{\bar{A}} = A - \frac{1}{2}q_D B_m \bar{R}^{-1} C_{D_{xu_m}}^T - q_M B_m \bar{R}^{-1} M_{u_m}^T M_x \tag{24}$$

$$\bar{\bar{Q}} = Q + q_D C_{D_{x^2}} + q_M M_x^T M_x - \left(\frac{1}{2}q_D C_{D_{xu_m}} + q_M M_x^T M_{u_m}\right)\bar{R}^{-1}\left(\frac{1}{2}q_D C_{D_{xu_m}}^T + q_M M_{u_m}^T M_x\right) \tag{25}$$

$$\bar{R} = R + q_D C_{D_{u^2 mm}} + q_M M_{u_m}^T M_{u_m} \tag{26}$$

References

[1] Nguyen, N., and Tal, E., “A multi-objective flight control approach for performance adaptive aeroelastic wing,"56th AIAA/ASCE/AHS/ASC Structures, Structural Dynamics, and Materials Conference, AIAA 2015-1843, January 2015.

[2] Hashemi, K.E. et al., “Performance optimizing gust load alleviation control of flexible wing aircraft," AIAA Guidance, Navigation, and Control Conference, AIAA 2018-0623, January 2018.

[3] Nguyen, N., “Elastically shaped future air vehicle concept," NASA Innovation Fund Award 2010 Report, October 2010, Submitted to NASA Innovative Partnerships Program, http://ntrs.nasa.gov/archive/nasa/casi.ntrs.nasa.gov/20110023698.pdf.

[4] Nguyen, N., Trinh, K., Reynolds, K., Kless, J., Aftosmis, M., Urnes, J., Ippolito, C., “Elastically shaped wing optimization and aircraft concept for improved cruise efficiency," AIAA Aerospace Sciences Meeting, AIAA 2013-0141, January 2013.

[5] Boeing Report No. 2012X0015, “Development of variable camber continuous trailing edge flap system," October 4, 2012.

[6] Rivers, M.B. and Dittberner, A., “Experimental Investigations of the NASA Common Research Model," *Journal of Aircraft*, Vol. 51, No. 4, July 2014, pp. 1183–1193.

[7] Cramer, N. and Nguyen, N., “Development of an aeroservoelastic model for gust load alleviation of the NASA Common Research Model wind tunnel experiment," AIAA SciTech, January 2020.

[8] Drew, M. et al., “Multi-objective gust load alleviation control designs for an aeroelastic wind tunnel demonstration wing," AIAA SciTech, January 2020.

[9] Stanford, B.K., “Optimal control surface layout for an aeroservoelastic wingbox," *AIAA Journal*, Vol. 55, No. 12, Dec 2017, pp. 4347-4356.

[10] Kammer, D.C., “Sensor placement for on-orbit modal identification and correlation of large space structures," *Journal of Guidance, Control, and Dynamics*, Vol. 14, No. 2, March 1991, pp. 251-259.